Supporting Information

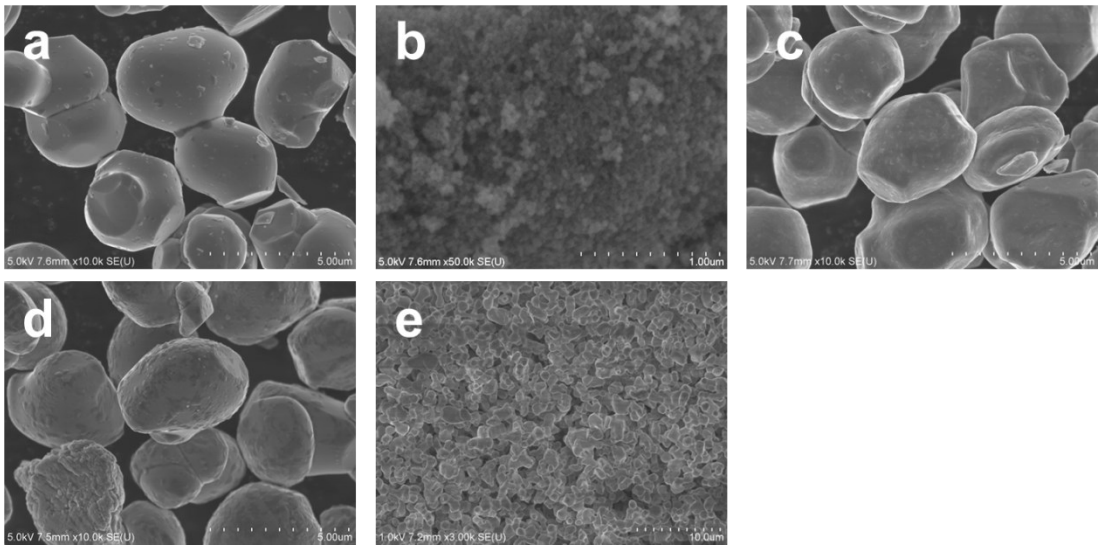

Fig. S1. FESEM image of a) bare LCO, b) nano-TiO_2, c) TiO_2-LCO, d) TiO_2@LCO (annealing the TiO_2-LCO without the presence of carbon and Li_2CO_3) and e) pure LCTO powder

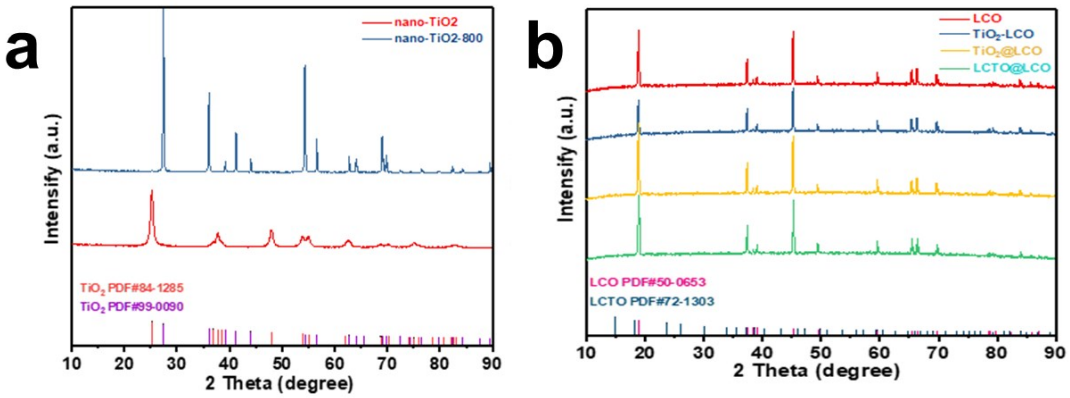

Fig. S2. a) XRD patterns of the nano-TiO_2 and nano-TiO_2-800 (heat treatment at 800 ºC). b) XRD patterns of the bare LCO, TiO_2-LCO, TiO_2@LCO and LCTO@LCO

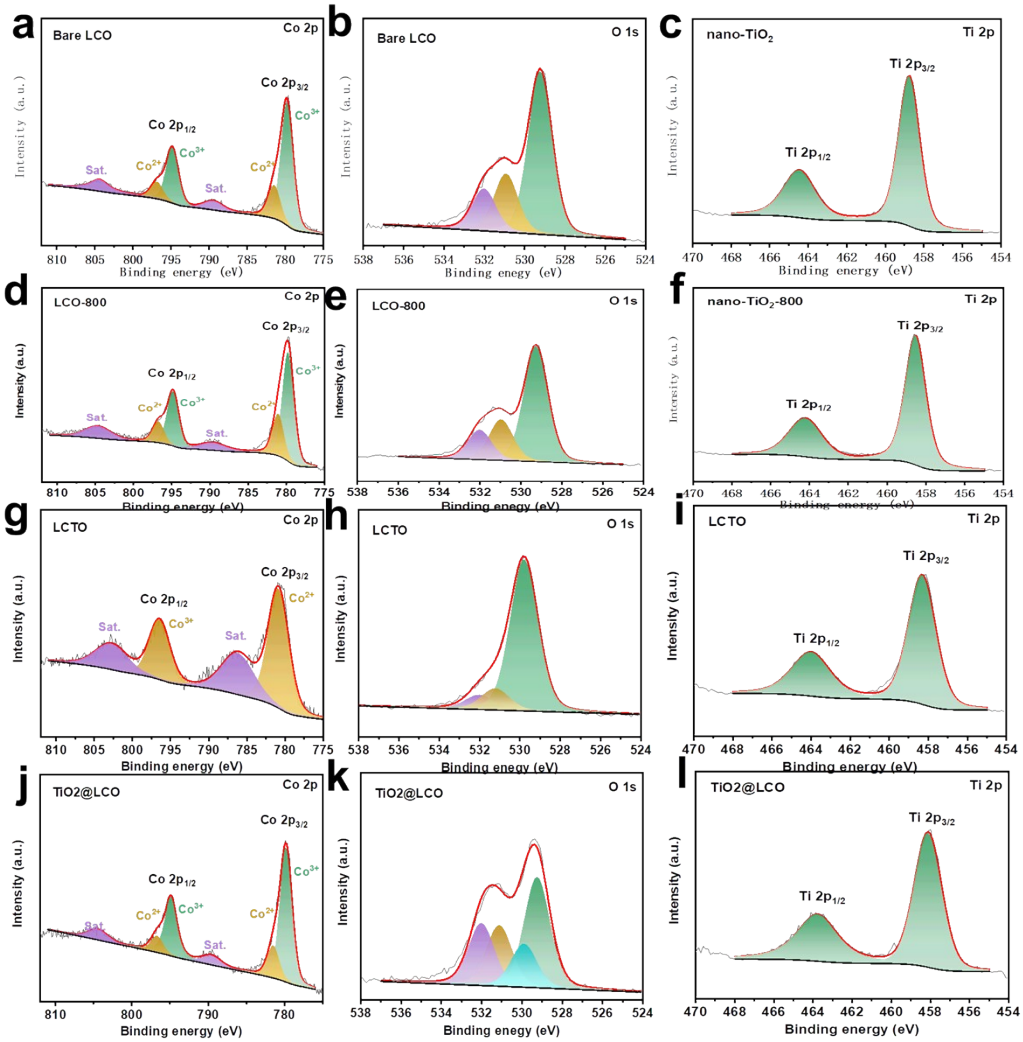

Fig. S3. XPS spectra of bare LCO, LCO-800, nano-TiO_2, nano-TiO_2-800, LCTO and TiO_2@LCO powder. Core-level XPS spectra of Co 2p (left), O 1s (middle), and Ti 2p (right).

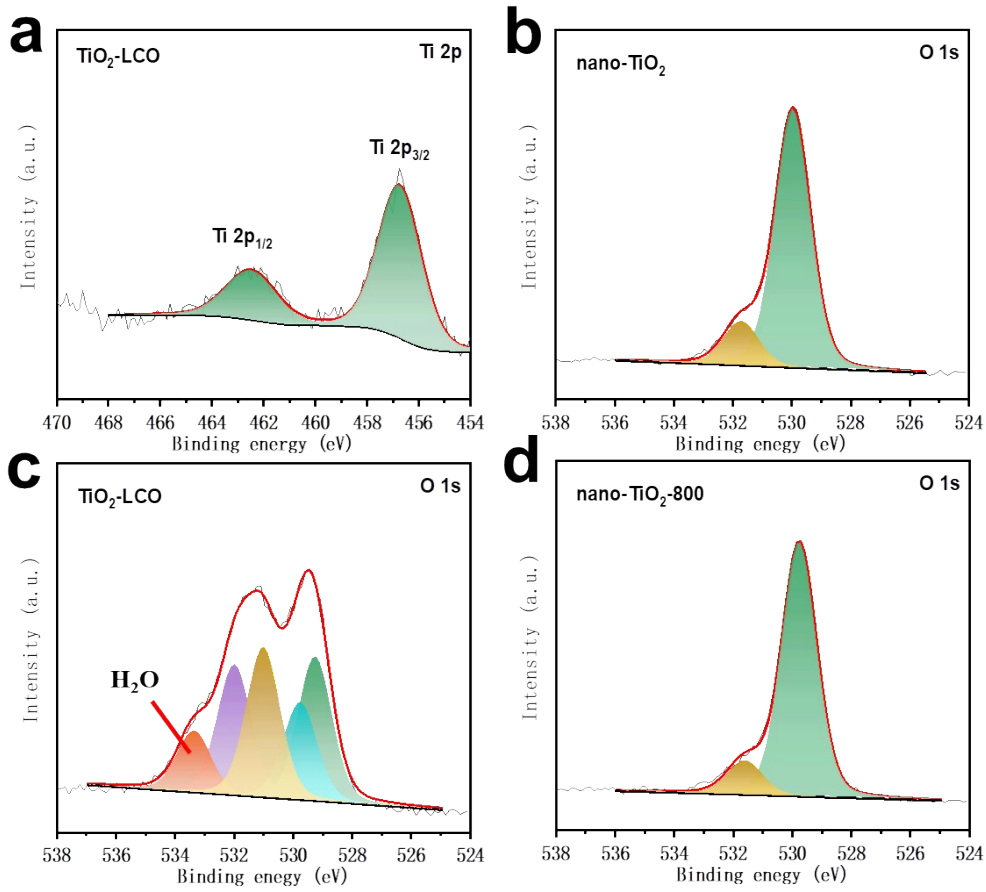

Fig. S4. a) Core-level XPS spectra of Ti 2p of TiO_2-LCO. Core-level XPS spectra of O 1s: b) nano-TiO_2, c) TiO_2-LCO and d) nano-TiO_2-800

Table S1. The summarization of the relative percentage of different oxygen species of different electrode materials

	O_{abs}%	O_{def} %	Ti-O%	Co-O%	*H_2O%
LCTO	7.8	21.8	50.0	20.4	—
pure LCO	17.6	41.4	—	48.3	—
LCO-800	21.2	28.6	—	56.2	—
TiO_2-LCO	21.9	25.5	15.4	25.3	11.9
LCTO@LCO	20.4	26.1	16.5	37.0	—
TiO_2@LCO	24.3	33.1	10.2	32.4	—

*Note that the appearance of H_2O-relevant oxygen species was found in the sample TiO_2-LCO **(Fig. S4c)**; this is because it has experienced a high speed mixing process that would inevitably change pristine surficial states of the bare LCO including the absorption of water in open air.

Table S2. The summarization of the relative percentage of Co^{2+} and Co^{3+} of different electrode materials

	Co $2p_{1/2}$ (%)			Co $2p_{3/2}$ (%)			Peak separation (eV)	
	Co(II)	**Co(III)**	**Sat.1**	**Co(II)**	**Co(III)**	**Sat.2**	**Co(II)**	**Co (III)**
LCTO	100	0	—	100	0	—	15.72	15.72
Bare LCO	40.7	59.3	66.5	31.6	68.4	47.0	15.22	15.04
LCO-800	41.9	58.1	56.9	31.5	68.5	36.7	15.32	15.06
LCTO@LCO	38.2	61.8	52.2	35.0	65.0	16.8	15.46	15.09
TiO_2@LCO	36.2	63.8	44.3	31.7	68.3	12.7	15.53	15.11

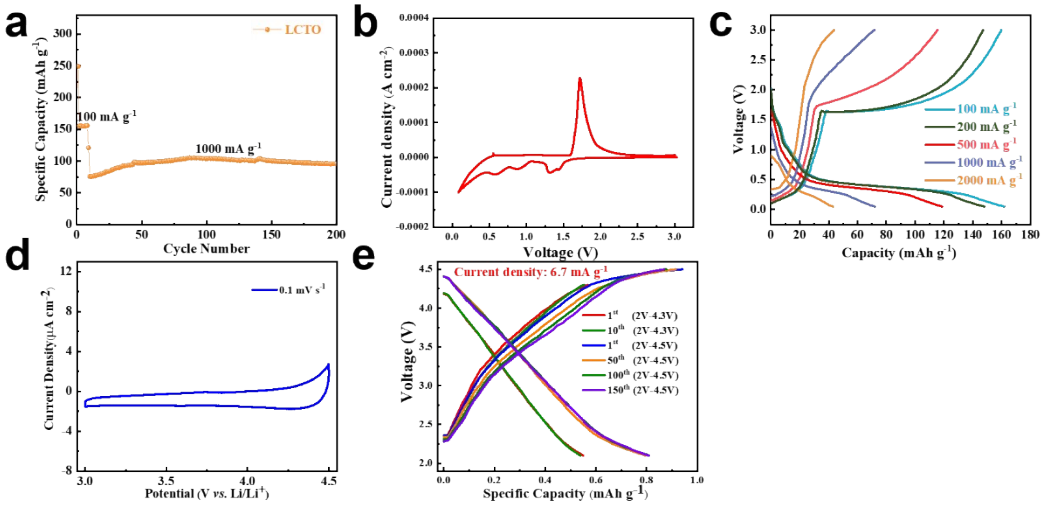

Fig. S5. a) Cycling performance of LCTO at high current density (1000 mA g^{-1}); b) CV profiles of the LCTO electrode at 1st sweeping; c) Charging-discharging curves of the LCTO electrode at different current densities. d) CV profiles of the LCTO electrode; e) Charging-discharging curves of the LCTO electrode at different current densities;

* From the electrochemical reaction of LCTO: $[LiCo_{0.9}]^{tetrahedron}[(LiCo_{0.1})Ti_3]^{octahedron}O_8+3e^-+3Li^+\rightarrow[Li_4]^{octahedron}[Co_{0.9}]^{tetrahedron}[(LiCo_{0.1})Ti_3]^{octahedron}O_8$, the number of electrons per molecule during the intercalation is 3; the concentration of lithium ions in crystal(C_0) is calculated to be 0.0226 mol cm^{-3}; the surface area of the electrode is replaced by geometric surface area of the electrode.

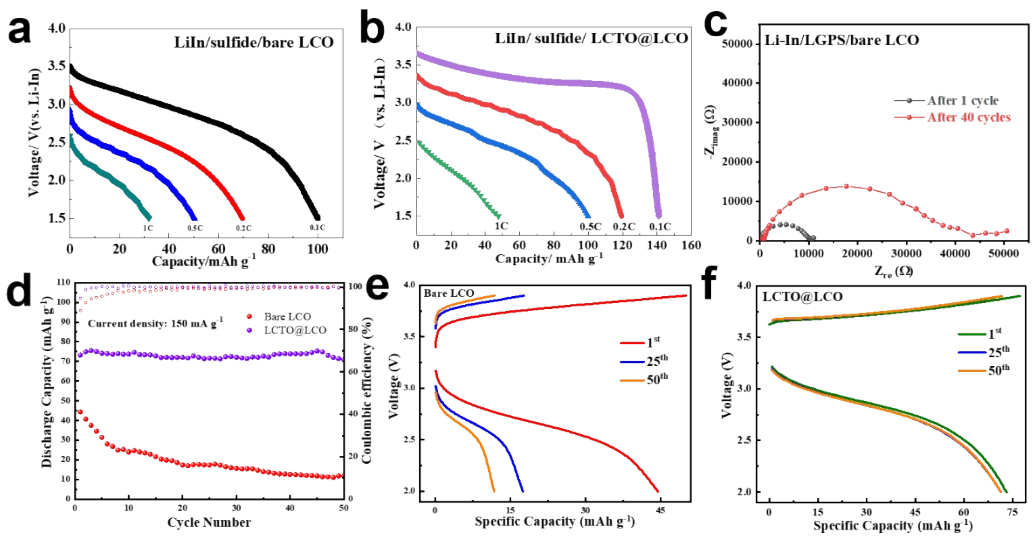

Fig. S6. Discharging curves of a) bare LCO and b) LCTO@LCO at different current densities, c) Nyquist plots of the bare LCO after the 1st and 40th cycles, d) Cycling stability and coulombic efficiency of bare LCO and LCTO@LCO at 1 C (150 mA g^{-1}); High-rate charge–discharge curves of e) the bare LCO and f) LCTO@LCO

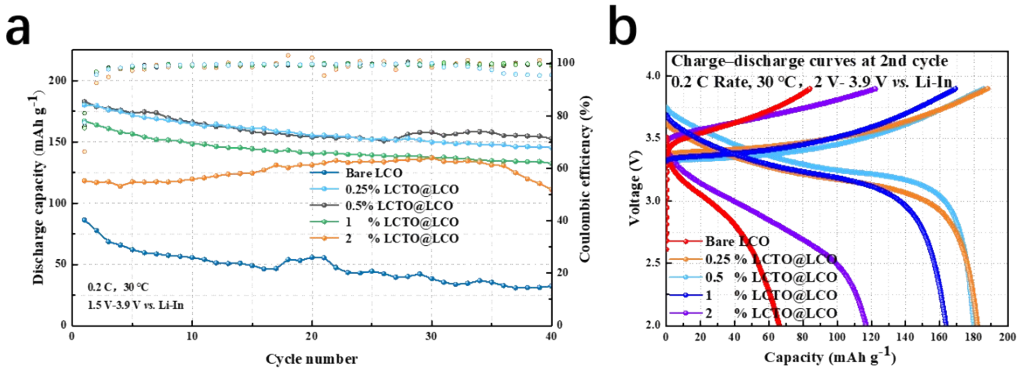

Fig. S7. Electrochemical performance of ASSLIBs with bare LCO, 0.25% LCTO@LCO, 0.5% LCTO@LCO, 1% LCTO@LCO and 2% LCTO@LCO: a) Cycling stability and coulombic efficiency, b) Charge–discharge curves at the 2nd cycle

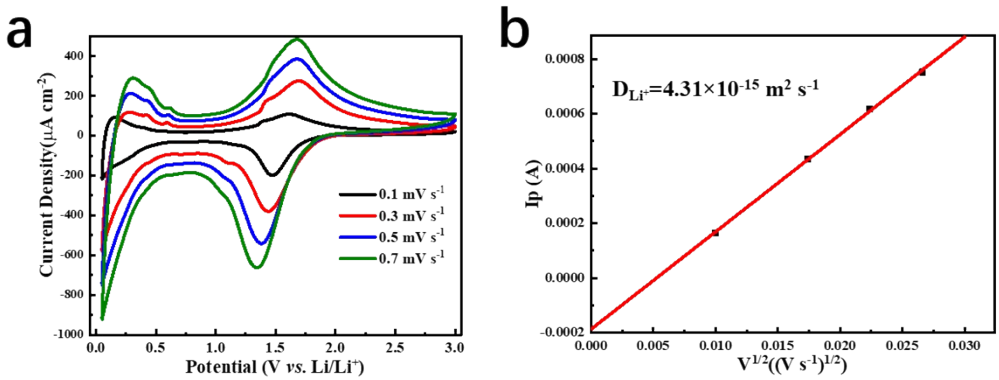

Fig. S8 a) CV profiles of the $LiNbO_3$ electrode with varying sweeping rates e) I_p–$v^{1/2}$ plots and the calculated D_{Li}^{+}.

Table S3 Phase equilibria and decomposition energies of the LGPS-LCO and LGPS-LCTO interfaces. x is the Molar Fraction of LGPS in [x·$Li_{10}GeP_2S_{12}$ + (1-x)·$Li_2CoTi_3O_8$/$LiCoO_2$]

Celectrode	x	Phase equilibria	$\Delta E_{D,\ total}$ (eV/mol)	$\Delta E_{D,mutual}$ (eV/atom)
$LiCoO_2$	0.01	$Li_{10}Co_4O_9$, Li_4GeO_4 CoO, Li_3PO_4, Li_2SO_4	-0.509	-0.121
	0.028	$Li_{10}Co_4O_9$, Li_4GeO_4, Li_3PO_4, Li_2SO_4, Co	-0.928	-0.202
	0.029	Li_6CoO_4, Li_4GeO_4, Li_3PO_4, Li_2SO_4, Co	-0.955	-0.207
	0.072	Li_6CoO_4, Li_4GeO_4, Co_9S_8, Li_3PO_4, Li_2SO_4	-1.668	-0.302
	0.08	Li_4GeO_4, Co_9S_8, Li_3PO_4, Li_2SO_4, Li_2O	-1.790	-0.315
	0.104	Li_4GeO_4, Co_9S_8, Li_3PO_4, Li_2SO_4, Li_2S	-2.122	-0.344
	0.112	Li_2GeO_3, Co_9S_8, Li_3PO_4, Li_2SO_4, Li_2S	-2.176	-0.343
	0.143	Li_2GeO_3, Li_3PO_4, Li_2SO_4, Co_3S_4, Li_2S	-2.357	-0.337
	0.186	Li_4GeS_4, Li_3PO_4, Li_2SO_4, Co_3S_4, Li_2S	-2.603	-0.329
	0.2	Co_2S_3, Li_4GeS_4, Li_3PO_4, Li_2S	-2.650	-0.323
Li3CoTi2O8	0.071	$Li_4Ti_5O_{12}$, Li_2TiGeO_5, Co_9S_8, Li_2SO_4, Li_3PO_4, TiO_2	-1.100	-0.074
	0.077	Co_3S_4, $Li_4Ti_5O_{12}$, Li_2TiGeO_5, Co_9S_8, Li_3PO_4, TiO_2	-1.161	-0.078

	0.091	Co_3S_4, $Li_4Ti_5O_{12}$, Co_9S_8, Li_3PO_4, GeS_2	-1.269	-0.085
	0.111	Co_3S_4, $Li_4Ti_5O_{12}$, Co_9S_8, Li_3PO_4, Li_4GeS_4, TiO_2	-1.337	-0.088
	0.333	Co_3S_4, $Li_4Ti_5O_{12}$, Li_3PO_4, $Li(TiS_2)_2$, Li_4GeS_4	-1.799	-0.102
	0.418	$Li_4Ti_5O_{12}$, Li_4TiS_4, Li_3PO_4, $Li(TiS_2)_2$, Li_4GeS_4, Co_2S_3	-1.944	-0.105
	0.5	Li_4TiS_4, TiS_3, Li_3PO_4, $Li(TiS_2)_2$, Li_4GeS_4, Co_2S_3	-2.081	-0.107

Table S4. EXAFS fitting parameters at the Co K-edge various samples（S_0^2=0.75）

Sample	Path	C.N.	R (Å)	$\sigma^2\times10^3$ (Å^2)	ΔE (eV)	R factor
Co foil	Co-Co	12*	2.50±0.01	6.4±0.2	7.8±0.3	0.001
Bare LCO	Co-O	5.5±0.7	1.92±0.01	2.7±0.9	-1.5±1.6	0.005
	Co-Co	5.5±0.6	2.82±0.01	2.6±0.6	-3.6±1.3	
LCTO@LCO	Co-O	6.0±0.9	1.90±0.01	1.9±1.0	-1.4±1.9	0.007
	Co-Co	5.3±0.7	2.81±0.01	1.2±0.7	-4.1±1.6	
LCTO@LCO cycled	Co-O	5.9±0.7	1.92±0.01	2.8±0.9	-1.6±1.6	0.005
	Co-Co	6.4±0.7	2.82±0.01	2.8±0.6	-3.7±1.3	

[a]*N*: coordination numbers; [b]*R*: bond distance; [c]σ^2: Debye-Waller factors; [d] ΔE_0: the inner potential correction. *R* factor: goodness of fit. * the experimental EXAFS fit of metal foil by fixing CN as the known crystallographic value.

Table S5 Lattice parameters of LCO, LGPS and LCTO obtained from first-principle calculation.

	LCO	LGPS	LCTO
Space group	$P\bar{1}$	P1	$P4_332$
a(Å)	2.8323	8.7882	8.37385
b(Å)			

c(Å)	14.1297	12.660

Table S6 Lattice parameters and interfacial work of adhesion of LCO/LGPS, LCO/LCTO and LCTO/LGPS interface obtained from first-principle calculation.

Interface	LCO/LGPS	LCO/LCTO	LCTO/LGPS
a(Å)	26.5733	26.0812	25.5825
b(Å)	8.6488	8.8511	8.5100
*W*ad (J m^{-2})	-0.39	-0.59	-0.55

Table S7 Comparison of lithium diffusion coefficients

Compound	Structure Type	D_{Li}($m^2 \cdot s^{-1}$)	T(K)	Reference
$Li_2CoTi_3O_8$	Spinel	8.22×10^{-11}	298	This work
$LiNbO_3$	$LiNbO_3$	4.31×10^{-15}	298	This work
$Li_{8.4}Nb_{16}W_5O_{55}$	Block,*cs*	1.6×10^{-13}	298	[1]
$Li_{3.4}Nb_{18}W_{16}O_{93}$	Bronze-like	1.1×10^{-13}	298	[1]
$Li_{10}GeP_2S_{12}$	Thio-LISICON	2×10^{-12}	298	[2]
Li_7GePS_8	Thio-LISICON	2×10^{-12}	298	[2]
$Li_{10}SnP_2S_{12}$	Thio-LISICON	1.4×10^{-12}	298	[3, 4]
$Li_7P_3S_{11}$	Thio-LISICON	$1\text{-}5\times10^{-12}$	303	[5]
amorphous-Li_3PS_4	Amorphous	6.5×10^{-13}	303	[6]
$Li_{0.6}[Li_{0.2}Sn_{0.8}S_2]$	Layered(O1)	$2\text{-}20\times10^{-12}$	298	[7]
$Li_{1.5}Al_{0.5}Ge_{1.5}(PO_4)_3$	NASICON	2.9×10^{-13}	311	[8]
$Li_{1.2}Al_{0.2}Ti_{1.8}(PO_4)_3$	NASICON	1.5×10^{-12}	250	[9]
$Li_7La_3Zr_2O_{12}$	Garnet	1.8×10^{-18}	298	[10]
$Li_4Ti_5O_{12}$	Spinel	3.2×10^{-15}	298	[11, 12]
$LiTi_2O_4$	Spinel	3.6×10^{-15}	298	[11]
Li_3NbO_4	Li_3NbO_4	4×10^{-21}	353	[13]
Li_3NbO_4	Li_3NbO_4	1×10^{-16}	553	[13]

Table S8. Bulk modulus and shear modulus of $LiCoO_2$, $Li_2CoTi_3O_8$, $Li_4Ti_5O_{12}$ and $LiNbO_3$

Compound	Bulk Modulus (K_{VRH})	Shear Modulus (G_{VRH})	Material Project ID
$LiCoO_2$	106.89 Gpa	67.41 Gpa	mp-755297
$Li_2CoTi_3O_8$	138.67 Gpa	91.54 Gpa	mp-768110
$Li_4Ti_5O_{12}$	108 Gpa	60 Gpa	mp-685194
$LiNbO_3$	102 Gpa	57 Gpa	mp-3731

Reference

1. K. J. Griffith, K. M. Wiaderek, G. Cibin, L. E. Marbella and C. P. J. N. Grey, 2018, **559**, 556-563.
2. A. Kuhn, V. Duppel, B. V. J. E. Lotsch and E. ence, 2013, **6**, 3548-3552.
3. A. Kuhn, O. Gerbig, C. Zhu, F. Falkenberg, J. Maier and B. V. J. P. C. C. P. Lotsch, 2014, **16**.
4. M. Kaus, H. Stöffler, M. Yavuz, T. Zinkevich, M. Knapp, H. Ehrenberg and S. J. T. J. o. P. C. C. Indris, 2017, **121**, 23370-23376.
5. K. Hayamizu and Y. J. S. S. I. Aihara, 2013, **238**, 7-14.
6. K. Hayamizu, Y. Aihara, T. Watanabe, T. Yamada, S. Ito and N. J. S. S. I. Machida, 2016, **285**, 51-58.
7. T. Holzmann, L. Schoop, M. Ali, I. Moudrakovski, G. Gregori, J. Maier, R. Cava, B. J. E. Lotsch and E. Science, 2016, **9**, 2578-2585.
8. K. Hayamizu and S. J. P. C. C. P. Seki, 2017, **19**, 23483-23491.

9. K. Arbi, I. Sobrados, M. Hoelzel, A. Kuhn, F. Garcia-Alvarado and J. J. M. O. P. L. A. Sanz, 2011, **1313**.

10. A. Kuhn, S. Narayanan, L. Spencer, G. Goward, V. Thangadurai and M. J. P. R. B. Wilkening, 2011, **83**, 094302.

11. J. Sugiyama, H. Nozaki, I. Umegaki, K. Mukai, K. Miwa, S. Shiraki, T. Hitosugi, A. Suter, T. Prokscha and Z. J. P. R. B. Salman, 2015, **92**, 014417.

12. J. Sugiyama, I. Umegaki, T. Uyama, R. M. McFadden, S. Shiraki, T. Hitosugi, Z. Salman, H. Saadaoui, G. D. Morris and W. A. J. P. R. B. MacFarlane, 2017, **96**, 094402.

13. B. Ruprecht and P. J. D. F. Heitjans, 2010, **12**, 100.